UC Santa Barbara
UC Santa Barbara Previously Published Works

Title
Direct observation of valley-coupled topological current in MoS_2

Permalink
https://escholarship.org/uc/item/8mx717dp

Journal
Science Advances, 5(4)

ISSN
2375-2548

Authors
Hung, Terry YT
Camsari, Kerem Y
Zhang, Shengjiao
et al.

Publication Date
2019-04-05

DOI
10.1126/sciadv.aau6478

Peer reviewed

eScholarship.org Powered by the California Digital Library
University of California

PHYSICS

Direct observation of valley-coupled topological current in MoS_2

Terry Y. T. Hung[1,2], Kerem Y. Camsari[1], Shengjiao Zhang[1,2], Pramey Upadhyaya[1], Zhihong Chen[1,2]*

Copyright © 2019 The Authors, some rights reserved; exclusive licensee American Association for the Advancement of Science. No claim to original U.S. Government Works. Distributed under a Creative Commons Attribution NonCommercial License 4.0 (CC BY-NC).

The valley degree of freedom of electrons in two-dimensional transition metal dichalcogenides has been extensively studied by theory (*1–4*), optical (*5–9*), and optoelectronic (*10–13*) experiments. However, generation and detection of pure valley current without relying on optical selection have not yet been demonstrated in these materials. Here, we report that valley current can be electrically induced and detected through the valley Hall effect and inverse valley Hall effect, respectively, in monolayer molybdenum disulfide. We compare temperature and channel length dependence of nonlocal electrical signals in monolayer and multilayer samples to distinguish the valley Hall effect from classical ohmic contributions. Notably, valley transport is observed over a distance of 4 μm in monolayer samples at room temperature. Our findings will enable a new generation of electronic devices using the valley degree of freedom, which can be used for future novel valleytronic applications.

INTRODUCTION

Electronic devices exploring carrier transport with spin and valley degree of freedom (DOF) have emerged as promising candidates for next-generation information storage and transport, because pure spin and valley currents do not accompany energy dissipation associated with Joule heating. The ability to electrically generate and detect these pure spin and valley currents in these devices is of particular importance. Over the past decade, driven by the emergence of the spin-orbit coupling engineering, tremendous experimental progress has been made to efficiently generate spin currents by electric currents. On the other hand, electrical control of the valley DOF has just started to attract interest in the past few years, initiated by theoretical studies of valleytronics in two-dimensional honeycomb lattice systems, such as gapped graphene and transition metal dichalcogenides (TMDs) (*1–4*, *14*, *15*), revealing the interplay of their unique band structures and topologies. Experimentally, topological valley transport has been observed in graphene systems when a superlattice structure or perpendicular electric field is used to break the inversion symmetry of this zero-bandgap semiconductor (*16–18*).

In contrast, monolayer TMDs, such as molybdenum disulfide (MoS_2), is a direct bandgap semiconductor. Electronic transport in these materials is dominated by the inequivalent K and K' valleys of the Brillouin zone located at band edges. Because of the inherent absence of inversion symmetry in monolayer TMDs, carriers in these two valleys have nonzero Berry curvature (Ω) without needing the assistance of external mechanisms to break the symmetry as in graphene systems. K and K' valleys are related by time-reversal symmetry, which forces the Berry curvature to flip its sign, i.e., $\Omega(K) = -\Omega(K')$, and allows optical selection through optical pumping of valley polarization (*5–7*). Ω acts as a pseudo-magnetic field in the momentum space and results in an anomalous transverse velocity in the presence of an electric field, i.e., $\nu_\perp = -\frac{e}{\hbar}E \times \Omega(k)$. Consequently, carriers from K and K' valleys develop opposite $\nu_\perp$, providing a route to electrically generate pure valley currents transverse to the applied electric field. This so-called valley Hall effect (VHE) has been used by Mak *et al.* (*10*) in monolayer MoS_2 devices to measure valley polarization created by circularly polarized light and has successfully generated polarization in gated bilayer MoS_2 that was then visualized by Kerr rotation microscopy (*11*). It is important to note that this unique VHE phenomenon would not appear in thick multilayer MoS_2 devices, because inversion symmetry is completely protected in samples with even layers and starts to recover in thick odd-layer samples (*19*). In addition, carrier transport in these indirect bandgap multilayer samples does not involve K and K' valleys, which can result in very small or even zero Berry curvature. In our experiments, we use multilayer MoS_2 devices as direct comparison or control samples to monolayer devices. Figure 1A illustrates the VHE occurring in the left vertical electrode of a monolayer MoS_2 Hall bar device. Analogous to the spin current, this valley current consists of carriers of opposite (valley) polarization moving along opposite directions, resulting in charge-neutral valley current along the x axis. Onsager reciprocity (*20*) then ensures the reciprocal effect, a phenomenon defined as the inverse VHE (iVHE) that converts a nonzero valley current into a transverse electric field, and finally develops charge accumulation across the right vertical electrode of the Hall bar in Fig. 1A. Here, we demonstrate electrical generation and detection of valley current in monolayer MoS_2 by combining VHE and iVHE in the above-described nonlocal Hall bar device geometry. We observe large nonlocal signals at distances more than 4 μm away from the charge current path and a unique temperature dependence that is consistent with valley transport physics.

RESULTS AND DISCUSSIONS

A colored scanning electron microscopy image of one of the measured MoS_2 Hall bar devices is shown in Fig. 1C. Two types of measurements can be made, as illustrated in Fig. 1B. A conventional four-probe measurement (type II) allows the extraction of sheet resistance and contact resistance, while the nonlocal setup (type I) measures the Hall voltage induced by any carrier distributions due to the VHE or classical ohmic contribution. A back-gate voltage (V_g) is applied to the SiO_2/Si substrate to modulate the carrier concentration in the MoS_2 channel. Device fabrication is provided in Materials and Methods. Optical and electrical characterizations and measurement details are provided in section S1. Typical n-type MoS_2 field-effect transistor behaviors are observed in two-probe measurements of all devices; sheet and contact

[1]School of Electrical and Computer Engineering, Purdue University, West Lafayette, IN 47907, USA. [2]Birck Nanotechnology Center, Purdue University, West Lafayette, IN 47907, USA.
*Corresponding author. Email: zhchen@purdue.edu

resistances are extracted from type II measurements for various temperatures ranging from 4 to 300 K (see section S1). Field-effect mobility values of ~10 and ~30 cm^2/Vs are typically measured at room temperature for monolayer and multilayer devices, respectively.

The most important spurious signal to be ruled out in our measurements is the ohmic contribution that can result in a van der Pauw–like signal (*21*) in a typical nonlocal type I measurement. When a DC bias of V_{ds} = 5 V is applied to the left electrode of the Hall bar, a nonlocal Hall voltage (V_{nl}) measured in the on-state of a monolayer MoS_2 device (40 V < V_g < 60 V) can reach ~0.6 V at T = 300 K and increase to ~1.2 V at T = 4 K, as compared to ~10- to 50-mV V_{nl} readings in the on-state of a multilayer (~9 to 10 layers) device (20 V < V_g < 40 V), as shown in Fig. 2 (A and C). As mentioned above, VHE does not exist in thick multilayer MoS_2 because inversion symmetry is either preserved or weakly broken and transport does not occur in K and K' valleys. Therefore, the detected finite V_{nl} signals in multilayer devices can only be associated with the ohmic contribution or any other unknown effects. The magnitude of the nonlocal voltage due to the ohmic contribution is expected to be dependent on the sheet resistance (ρ_{sh}) of the channel and device geometry: $V_{\text{ohmic}} = I_{\text{DC}}\rho_{\text{sh}}\frac{W}{W_1}e^{\frac{-\pi L}{W}}$ (*21*), where L is the channel length and W and W_1 are the width of the channel and the current electrode, respectively (labeled in Fig. 1A). Using individual I_{DC} and ρ_{sh} measured for monolayer and multilayer MoS_2, we are able to calculate the ohmic contribution as a function of the back-gate voltage (V_g) for each device, as presented in Fig. 2 (B and D). We notice that the magnitude of the measured V_{nl} of the multilayer device from Fig. 2C matches the values of the calculated ohmic contribution, while more than one order of magnitude larger V_{nl} signals are measured in the monolayer MoS_2 device with an opposite temperature trend that we will discuss later. This significant magnitude difference in measured nonlocal voltages is also supported by a detailed potential analysis that resembles our experimental setup, as shown in Fig. 3. Using experimentally measured contact resistance and MoS_2 sheet resistance obtained from the four-probe measurement, only a fraction of the supply voltage (V_{ds} = 5 V) is actually applied across the injector lead, i.e., V_{in} = 1.8 V. We then simulate in SPICE a resistor network with 4×10^6 identical resistors uniformly distributed over the Hall bar and observe that when a constant voltage of 1.8 V is applied at the injector, the nonlocal voltage drop across the detector lead in the given geometry due to the ohmic contribution is expected to be ~29 mV. This picture can get more complicated by the gate field–controlled Schottky barrier contacts (*22*). Nevertheless, we conclude that the magnitude of V_{nl} due to the ohmic contribution calculated from the resistor network is in good agreement with the experimental measurements in multilayer MoS_2 devices. We benchmark

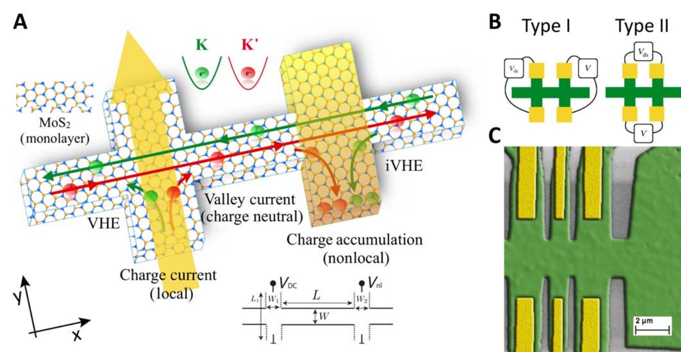

Fig. 1. Valley-coupled topological current. (**A**) Schematic of valley-coupled topological current due to VHE and iVHE in monolayer MoS_2 and the device geometry (bottom), where W_1 = 1 μm, $W = W_2$ = 2 μm, L_1 = 4.5 μm, and L = 0.5 μm. (**B**) Schematics of two measurement setups: type I and type II. (**C**) Patterned MoS_2 flake (green) and lithographically defined metal electrodes (yellow).

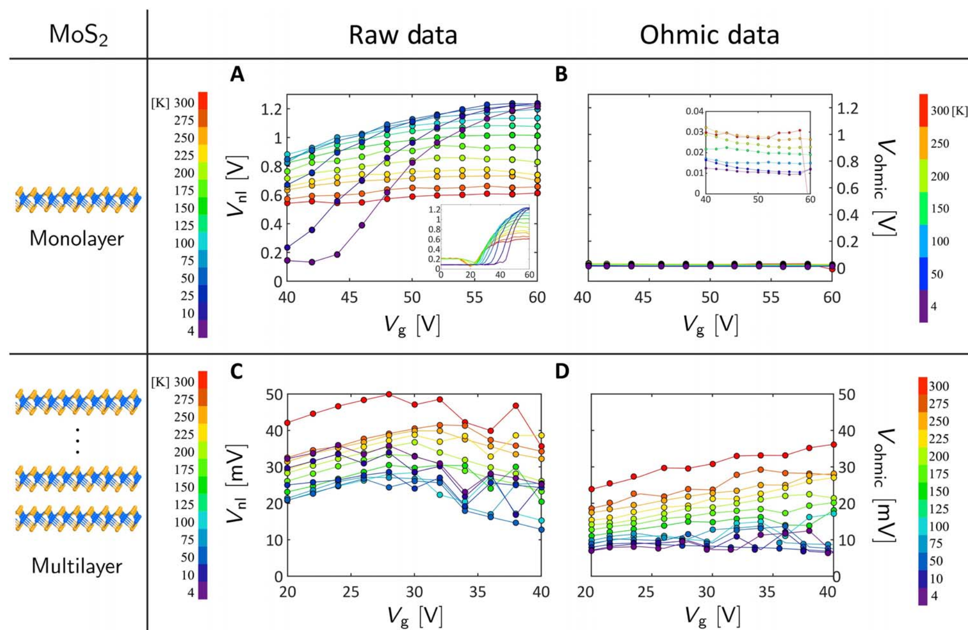

Fig. 2. Comparison of nonlocal voltages obtained in monolayer and multilayer MoS_2 devices. (**A**) Measured nonlocal voltage with respect to global back-gate voltage V_g in monolayer MoS_2 using type I setup. Inset: Full range of V_g. Note that data points in the range of V_g < 40 V are not included in analysis because these large device resistances become comparable to the input impedance of the nanovoltmeter. (**B**) Ohmic contribution calculated from the measured sheet resistance: $V_{\text{ohmic}} = I_{\text{DC}}\rho_{\text{sh}}\frac{W}{W_1}e^{\frac{-\pi L}{W}}$ as a function of V_g, plotted with the same y-axis range as in (A). Inset: Zoom-in data. (**C** and **D**) Nonlocal voltage response in a multilayer MoS_2 device for the same measurements performed in (A) and (B). Note that the y axis in both plots has a unit of millivolts.

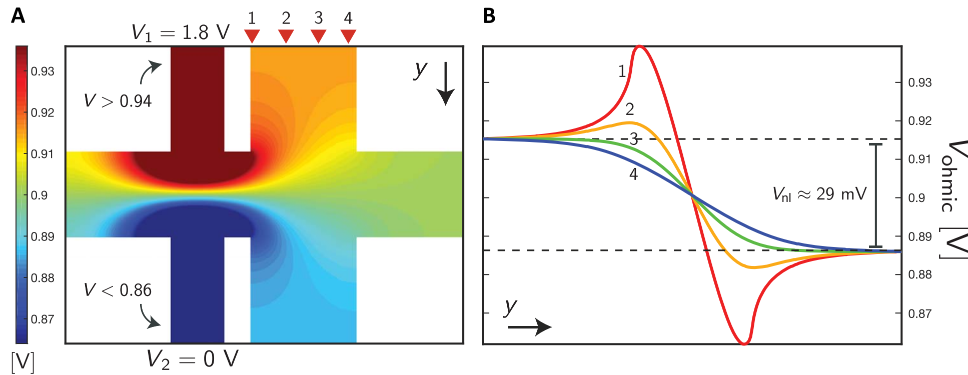

Fig. 3. Electric potential mapping from a SPICE-based resistor network simulation. (**A**) SPICE simulation of a resistor grid with ~4 × 10^6 uniform resistors, where each resistor corresponds to ~3-nm channel length, with (x = 1500, y = 1400) points. V_{ds} values applied at the two ends of the injector are V_1 = 1.8 V and V_2 = 0 V, respectively. Values greater than 0.94 V and less than 0.86 V are denoted with the same colors to resolve the nonlocal voltage distribution. (**B**) Voltage profiles along the y direction for four different positions denoted by arrows (1 to 4) in (A). Nonlocal voltage difference under open circuit condition is calculated to be ~29 mV.

the SPICE-based resistor network simulation with the analytical equation in section S2. We also rule out the possibility of magnitude difference coming from the characteristic difference between monolayer and multilayer by evaluating the impact of mobilities on nonlocal signals (see section S1).

In addition to the magnitude of V_{nl}, its temperature dependence provides further evidence in support of the VHE being responsible for the nonlocal carrier transport in monolayer MoS_2. Figure 4A shows increasing V_{nl} with decreasing temperature down to 50 K in monolayer MoS_2, while a completely opposite trend is observed for the multilayer in Fig. 4B. Note that, because a voltage source (V_{ds}) is used in our measurements (instead of a constant current source), the temperature dependence of V_{ohmic} due to the sheet resistance (ρ_{sh}) is expected to be cancelled out. However, finite contact resistance (R_c) needs to be considered in all MoS_2 devices, which prevents ρ_{sh} to be eliminated in the evaluation of the ohmic contribution. It is expected that $V_{ohmic} = \frac{V_{ds}}{\left(2R_C+\rho_{sh}\frac{L_1}{W_1}\right)}\rho_{sh}\frac{W}{W_1}e^{\frac{-\pi L}{W}}$. Different temperature dependences of R_c and ρ_{sh} are observed in four-probe measurements, as presented in section S1. The increasing V_{nl} with increasing temperature observed in Fig. 4B for the multilayer MoS_2 device (dots) can be fitted by the modified V_{ohmic} equation, considering the contribution from the contact resistance (lines). On the other hand, the increasing V_{nl} with decreasing temperature down to 50 K for the monolayer MoS_2 device is expected for enhanced intervalley scattering length (λ) at low temperatures (*9*, *23*, *24*), confirming that valley transport is responsible for the observed large signals. More detailed analyses of nonlocal signals and intervalley scattering length will be discussed in the following section.

This increasing V_{nl} with decreasing temperature trend stops at T ~ 50 K and reaches its maximum value. This unique maximum point results from two extreme limits of λ approaching either zero or infinity. While smaller V_{nl} is expected with increasing temperature due to a shorter λ, large λ at temperatures lower than 50 K can also lead to reduced nonlocal resistances, $R_{nl} = V_{nl}/I_{DC}$. This transition can actually be analogized to the well-studied quenched Hall effect (*25*, *26*), where the Hall voltage vanishes when the carriers' longitudinal velocity is much higher than the transverse velocity. We suggest that the observed nonmonotonic temperature dependence of V_{nl} for monolayer MoS_2 is an outcome of the monotonically increasing λ with decreasing temperature. We highlight that this temperature dependence of λ is consistent with the recent observation of increased intervalley scattering rate at higher temperatures in TMDs, which is attributed to phonon-activated intervalley relaxation (*27*).

We will now quantitatively analyze this interesting temperature dependence of R_{nl} for monolayer MoS_2 using a self-consistent theoretical model describing the VHE. This model, similar to other theoretical descriptions in the literature (*18*, *21*), assumes a uniform and rectangular geometry without considering the arm lengths (Fig. 4C). Also following (*18*, *21*), we use a circuit model that is equivalent (*28*, *29*) to the standard spin-diffusion equation used in the context of materials with spin Hall effect to describe the VHE by defining the valley Hall angle as $\theta = \sigma_{xy}/\sigma_{xx}$, where σ_{xx} and σ_{xy} denote longitudinal and transverse Hall conductivities, respectively. The valley Hall conductivity includes both intrinsic and extrinsic contributions and can be written as $\sigma_{xy} = \sigma_{xy}^{in} + \sigma_{xy}^{ex}$ (*30*). When the Fermi level lies close to the conduction band minima, a condition that is fulfilled by our MoS_2 devices (see section S7), σ_{xy}^{in}, dominates over σ_{xy}^{ex} (*30*). Using $\sigma_{xy}^{in} \sim \frac{2e^2}{h}$ (*16*) and measured σ_{xx}, we estimate θ ~ 0.4 at T = 50 K for our devices, which is similar to the estimation of Gorbachev *et al.* (*16*) (see section S7 for a detailed calculation of θ as a function of temperature). As also noted in (*18*), when θ is not small (i.e., θ ~ 1), one needs to self-consistently solve R_{nl}, considering the feedback impact of iVHE that behaves as a load to the generating section (induced by the direct VHE) and the impact of VHE that serves as a load to the detecting section (governed by the iVHE). Our circuit model automatically captures these self-consistencies to arbitrary order when solved in SPICE, but it is possible to derive an analytical equation considering only the iVHE at the generator side and the VHE at the detector side as second-order effects. Furthermore, our model takes the width of the arms explicitly, and we can analytically obtain the following expression for the nonlocal resistance (see section S3 for a detailed derivation)

$$R_{nl} \equiv \frac{V_{nl}}{I_{DC}} = \frac{2\rho\lambda W \exp\left[-\frac{L}{\lambda}\right]\sinh\left[\frac{W_1}{2\lambda}\right]\sinh\left[\frac{W_2}{2\lambda}\right]\theta^2}{\left(\exp\left[\frac{W_1}{2\lambda}\right]W_1 + 2\lambda\sinh\left[\frac{W_1}{2\lambda}\right]\theta^2\right)\left(\exp\left[\frac{W_2}{2\lambda}\right]W_2 + 2\lambda\sinh\left[\frac{W_2}{2\lambda}\right]\theta^2\right)} \quad (1)$$

where λ is the intervalley scattering length; W_1 and W_2 are the widths of the generating and detecting arm, respectively; ρ_{sh} is the sheet resistance; and W is the width of the channel in Fig. 4C. We combine

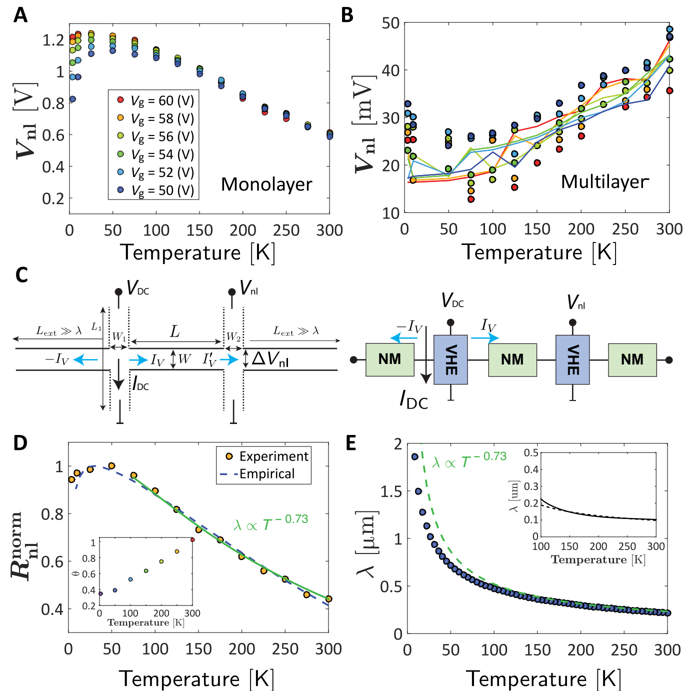

Fig. 4. Temperature dependence and extraction of intervalley scattering length. (**A**) Measured V_{nl} as a function of temperature at different V_g for monolayer MoS_2. (**B**) Temperature dependence of multilayer MoS_2 at different V_g (dots) and the calculated trends (lines) using the modified ohmic equation, $V_{ohmic} = \frac{V_{ds}}{\left(2R_C+\rho_{sh}\frac{L_1}{W_1}\right)}\rho_{sh}\frac{W}{W_1}e^{\frac{-\pi L}{W}}$, with the consideration of the contact resistance contribution (see section S1). Note that the trends of V_{nl} with respect to temperature in (A) and (B) are completely opposite. (**C**) Device geometry and corresponding valley-circuit model that define the geometric parameters in Eq. 1. Details are given in section S3. (**D**) Temperature dependence of R_{nl}^{norm} (normalized to the maximum point) measured at V_g = 58 V [orange dots in (A)]. The empirical fittings use $\lambda(T) = 5.5T^{-0.47} - 0.16$ (dashed blue line) and $\lambda = 15T^{-0.73}$ at $T > 100$ K (green line). Inset: Calculated temperature dependence of valley Hall angle, θ. (**E**) λ (T) extracted from R_{nl} and the power-law dependence described in (D). Inset: Theoretically calculated intervalley scattering length (solid line) and $\lambda \propto T^{-0.6}$ to guide the eye (dashed line).

our VHE model (*29*) with nonmagnetic circuit models that are also derived from a valley-diffusion equation (without any spin-orbit coupling) to obtain the infinite valley loads on both ends, as well as to obtain the valley diffusion in the middle channel whose length is denoted by L, based on the spin-circuit modeling described in (*28*). Conversely, the VHE model only considers charge transport in the vertical direction and valley-coupled topological current in the longitudinal direction. It is important to note that Eq. 1 is validated by a self-consistent numerical simulation of the composite valley circuit in SPICE simulations and can be analytically reduced to the expression generally used in the literature (*21*), if we assume $\theta^2 \ll 1$ and $W_{1,2}/\lambda \ll 1$, yielding $R_{nl} = \frac{1}{2}\left(\theta^2 \frac{W}{\sigma\lambda}\right) \exp\left(\frac{-L}{\lambda}\right)$. It is clear from the complete (Eq. 1) and reduced equation that the two extreme limits of λ naturally lead to an optimal intervalley scattering length to reach the maximum nonlocal resistance value.

This unique behavior enables us to quantitatively extract λ. As suggested by Eq. 1, the temperature dependence of R_{nl} comes from that of λ and θ. With the calculated θ (T) shown in the inset of Fig. 4D (section S7), we are able to fit the normalized nonlocal resistance, R_{nl}^{norm} curve (dashed blue line in Fig. 4D, labeled as "Empirical") by tuning λ (T). Because different physical mechanisms are responsible for the decreasing R_{nl}^{norm} in the low and high temperature regimes, we can separately fit the high temperature trend with a power-law function of $\lambda \propto T^{-0.73}$, which is in line with the temperature dependence of intervalley scattering that will be discussed later. Fitting for $T > 75$ K regime is shown as the solid green line in Fig. 4D. λ (T) is then quantitatively extracted from R_{nl}^{norm} and plotted (blue dots) in Fig. 4E, in a good agreement with the power-law fitting at high temperatures. Furthermore, using the analytical expression in (*31*) describing both acoustic and optical intervalley phonon scattering together with the field-effect mobility extracted from type II measurements, we are able to analytically derive λ (T) as shown by the solid line in the inset of Fig. 4E (see sections S1 and S8). A power-law fitting of $\lambda \propto T^{-0.6}$ (dashed line) is obtained here, which is consistent with the experimental fitting of $\lambda \propto T^{-0.73}$ at $T > 100$ K. At low temperatures, the extraction of λ > 1 μm from the experimentally measured nonlocal signals is comparable to other valley Hall systems, as reported in (*16*–*18*).

In addition to this unique λ extraction through fitting the temperature dependence plot, three distinguished long-channel devices were fabricated on the same monolayer MoS_2 flake to allow λ extraction through the channel length dependence (see section S6). Nonlocal signals larger than ~450 mV were observed at room temperature for the device with L = 2 μm and ~120 mV for L = 4 μm, and finally diminish when the channel is 5.5 μm long. λ ~ 600 nm is extracted for valley transport at room temperature, which is consistent with the temperature fitting method within a reasonable range considering sample-to-sample variations. In general, λ is believed to be governed at low temperatures by atom-like defects that provide the necessary momentum required for carriers to scatter between K and K' valleys in the conduction band. In MoS_2, these atom-like defects arise due to molybdenum and sulfur vacancies. Recently, it has been pointed out that owing to the symmetry of atomic defects, only molybdenum vacancies can participate in intervalley scattering (*32*). Fourier transform scanning tunneling spectroscopy studies also provide further evidence (*33*, *34*). The relatively large λ on the micrometer scale extracted from our devices could be a result of relatively low molybdenum vacancy density in our MoS_2 sample.

Last, nonlocal signals measured with in-plane magnetic field applied up to 5 T are presented in section S10. As expected, no impact from the magnetic field is observed, indicating the robustness of the valley polarization in monolayer MoS_2 and further excluding the possibility that the spin Hall effect is responsible for our measurements. Therefore, these results once again resonate with the mechanism of the VHE (*5*, *35*).

In summary, we report electrically generating and detecting valley-coupled topological current in monolayer MoS_2. Our approach provides a unique way to integrate charge, spin, and valley DOFs, which can be useful for emerging device technologies.

MATERIALS AND METHODS

Device fabrication

Chemical vapor deposition (CVD)–grown MoS_2 films were transferred to 90-nm SiO_2 substrates with highly doped Si on the back side serving as a global back gate (V_g). The transfer process includes the following: (i) The sample was spin-coated with polystyrene (PS) followed by immersion in deionized (DI) water, (ii) the PS/MoS_2 stack was then detached from the substrate and scooped up by the receiving SiO_2 substrate, and (iii) PS was subsequently dissolved by toluene and bathed in acetone and isopropyl alcohol to thoroughly clean it. Standard e-beam lithography

using poly(methyl methacrylate) (PMMA) A4 950 resist was used to pattern electric contacts on the CVD MoS_2 flakes. Ti/Au (20 nm/80 nm) was deposited in an e-beam evaporator followed by a liftoff process in acetone. The CVD-grown boron nitride (BN) film was transferred from Cu foil onto the devices through a process that involves etching the Cu foil with iron chloride ($FeCl_3$) and immersing it in diluted HCl and DI water alternatingly for a few times before scooping up. This BN layer was inserted to minimize device degradation from PMMA residues after the reactive ion etching (RIE) process. RIE etching mask was defined by e-beam lithography using PMMA A4 950 resist, and BN/MoS_2 flakes were etched using Ar/SF_6 for 10 s. The final devices were annealed in forming gas (N_2/H_2) at 300°C for 3 hours, followed by vacuum annealing (~10^{-8} torr) at 250°C for 4 hours to minimize PMMA residue and threshold voltage shift due to trap charges.

SUPPLEMENTARY MATERIALS

Supplementary material for this article is available at http://advances.sciencemag.org/cgi/content/full/5/4/eaau6478/DC1
Section S1. Optical and electrical characterizations
Section S2. Details of resistor network for ohmic contribution
Section S3. Derivation of nonlocal resistance, R_{nl}
Section S4. Additional nonlocal measurements for multilayer MoS_2 devices
Section S5. Additional nonlocal measurements from other monolayer MoS_2 devices
Section S6. Channel length and width dependence in monolayer MoS_2 device
Section S7. Detailed θ calculation and its temperature trend
Section S8. Detailed λ calculation and its temperature trend
Section S9. Nonlocal internal resistance measurements
Section S10. Applied in-plane magnetic field
Fig. S1. Device layer number confirmations.
Fig. S2. Device electrical characterizations.
Fig. S3. SPICE-based resistor network.
Fig. S4. The lumped valley-circuit model that is used to derive Eq. 1.
Fig. S5. Comparison of analytical equations for R_{nl} with the full SPICE simulation of the circuit shown in fig. S4.
Fig. S6. Long-channel multilayer MoS_2 devices and additional monolayer MoS_2 device measurements.
Fig. S7. Length dependence in monolayer MoS_2.
Fig. S8. Valley Hall angle and intervalley scattering length.
Fig. S9. Extraction of internal resistance in the nonlocal electrode.
Fig. S10. V_{nl} measurements with in-plane magnetic field applied.
References (*36–41*)

REFERENCES AND NOTES

1. D. Xiao, G.-B. Liu, W. Feng, X. Xu, W. Yao, Coupled spin and valley physics in monolayers of MoS2 and other group-VI dichalcogenides. *Phys. Rev. Lett.* **108**, 196802 (2012).
2. T. Cao, G. Wang, W. Han, H. Ye, C. Zhu, J. Shi, Q. Niu, P. Tan, E. Wang, B. Liu, J. Feng, Valley-selective circular dichroism of monolayer molybdenum disulphide. *Nat. Commun.* **3**, 887 (2012).
3. W. Yao, D. Xiao, Q. Niu, Valley-dependent optoelectronics from inversion symmetry breaking. *Phys. Rev. B* **77**, 235406 (2008).
4. W. Feng, Y. Yao, W. Zhu, J. Zhou, W. Yao, D. Xiao, Intrinsic spin Hall effect in monolayers of group-VI dichalcogenides: A first-principles study. *Phys. Rev. B* **86**, 165108 (2012).
5. H. Zeng, J. Dai, W. Yao, D. Xiao, X. Cui, Valley polarization in MoS_2 monolayers by optical pumping. *Nat. Nanotechnol.* **7**, 490–493 (2012).
6. K. F. Mak, K. He, J. Shan, T. F. Heinz, Control of valley polarization in monolayer MoS_2 by optical helicity. *Nat. Nanotechnol.* **7**, 494–498 (2012).
7. A. M. Jones, H. Yu, N. J. Ghimire, S. Wu, G. Aivazian, J. S. Ross, B. Zhao, J. Yan, D. G. Mandrus, D. Xiao, W. Yao, X. Xu, Optical generation of excitonic valley coherence in monolayer WSe_2. *Nat. Nanotechnol.* **8**, 634–638 (2013).
8. D. MacNeill, C. Heikes, K. F. Mak, Z. Anderson, A. Kormányos, V. Zólyomi, J. Park, D. C. Ralph, Breaking of valley degeneracy by magnetic field in monolayer MoSe2. *Phys. Rev. Lett.* **114**, 037401 (2015).
9. L. Yang, N. A. Sinitsyn, W. Chen, J. Yuan, J. Zhang, J. Lou, S. A. Crooker, Long-lived nanosecond spin relaxation and spin coherence of electrons in monolayer MoS_2 and WS_2. *Nat. Phys.* **11**, 830–834 (2015).
10. K. F. Mak, K. L. McGill, J. Park, P. L. McEuen, The valley Hall effect in MoS_2 transistors. *Science* **344**, 1489–1492 (2014).
11. J. Lee, K. F. Mak, J. Shan, Electrical control of the valley Hall effect in bilayer MoS_2 transistors. *Nat. Nanotechnol.* **11**, 421–425 (2015).
12. S. Wu, J. S. Ross, G.-B. Liu, G. Aivazian, A. Jones, Z. Fei, W. Zhu, D. Xiao, W. Yao, D. Cobden, X. Xu, Electrical tuning of valley magnetic moment through symmetry control in bilayer MoS_2. *Nat. Phys.* **9**, 149–153 (2013).
13. Y. Ye, J. Xiao, H. Wang, Z. Ye, H. Zhu, M. Zhao, Y. Wang, J. Zhao, X. Yin, X. Zhang, Electrical generation and control of the valley carriers in a monolayer transition metal dichalcogenide. *Nat. Nanotechnol.* **11**, 598–602 (2016).
14. D. Xiao, W. Yao, Q. Niu, Valley-contrasting physics in graphene: Magnetic moment and topological transport. *Phys. Rev. Lett.* **99**, 236809 (2007).
15. J. R. Schaibley, H. Yu, G. Clark, P. Rivera, J. S. Ross, K. L. Seyler, W. Yao, X. Xu, Valleytronics in 2D materials. *Nat. Rev. Mater.* **1**, 16055 (2016).
16. R. V. Gorbachev, J. C. Song, G. L. Yu, A. V. Kretinin, F. Withers, Y. Cao, A. Mishchenko, I. V. Grigorieva, K. S. Novoselov, L. S. Levitov, A. K. Geim, Detecting topological currents in graphene superlattices. *Science* **346**, 448–451 (2014).
17. M. Sui, G. Chen, L. Ma, W.-Y. Shan, D. Tian, K. Watanabe, T. Taniguchi, X. Jin, W. Yao, D. Xiao, Y. Zhang, Gate-tunable topological valley transport in bilayer graphene. *Nat. Phys.* **11**, 1027–1031 (2015).
18. Y. Shimazaki, M. Yamamoto, I. V. Borzenets, K. Watanabe, T. Taniguchi, S. Tarucha, Generation and detection of pure valley current by electrically induced Berry curvature in bilayer graphene. *Nat. Phys.* **11**, 1032–1036 (2015).
19. Y. Li, Y. Rao, K. F. Mak, Y. You, S. Wang, C. R. Dean, T. F. Heinz, Probing symmetry properties of few-layer MoS_2 and h-BN by optical second-harmonic generation. *Nano Lett.* **13**, 3329–3333 (2013).
20. P. Jacquod, R. S. Whitney, J. Meair, M. Büttiker, Onsager relations in coupled electric, thermoelectric, and spin transport: The tenfold way. *Phys. Rev. B Condens. Matter Mater. Phys.* **86**, 155118 (2012).
21. D. A. Abanin, A. V. Shytov, L. S. Levitov, B. I. Halperin, Nonlocal charge transport mediated by spin diffusion in the spin Hall effect regime. *Phys. Rev. B* **79**, 035304 (2009).
22. X. Cui, G. H. Lee, Y. D. Kim, G. Arefe, P. Y. Huang, C. H. Lee, D. A. Chenet, X. Zhang, L. Wang, F. Ye, F. Pizzocchero, B. S. Jessen, K. Watanabe, T. Taniguchi, D. A. Muller, T. Low, P. Kim, J. Hone, Multi-terminal transport measurements of MoS_2 using a van der Waals heterostructure device platform. *Nat. Nanotechnol.* **10**, 534–540 (2015).
23. X. Song, S. Xie, K. Kang, J. Park, V. Sih, Long-lived hole spin/valley polarization probed by Kerr rotation in monolayer WSe_2. *Nano Lett.* **16**, 5010–5014 (2016).
24. W. T. Hsu, Y. L. Chen, C. H. Chen, P. S. Liu, T. H. Hou, L. J. Li, W. H. Chang, Optically initialized robust valley-polarized holes in monolayer WSe_2. *Nat. Commun.* **6**, 8963 (2015).
25. H. U. Baranger, A. D. Stone, Geometrical effects on the Hall resistance in ballistic microstructures. *Surf. Sci.* **229**, 212–215 (1990).
26. C. J. B. Ford, S. Washburn, M. Büttiker, C. M. Knoedler, J. M. Hong, Influence of geometry on the Hall effect in ballistic wires. *Phys. Rev. Lett.* **62**, 2724–2727 (1989).
27. J. Kim, C. Jin, B. Chen, H. Cai, T. Zhao, P. Lee, S. Kahn, K. Watanabe, T. Taniguchi, S. Tongay, M. F. Crommie, F. Wang, Observation of ultralong valley lifetime in WSe_2/MoS_2 heterostructures. *Sci. Adv.* **3**, e1700518 (2017).
28. K. Y. Camsari, S. Ganguly, S. Datta, Modular approach to spintronics. *Sci. Rep.* **5**, 10571 (2015).
29. S. Hong, S. Sayed, S. Datta, Spin circuit representation for the spin Hall effect. *IEEE Trans. Nanotechnol.* **15**, 225–236 (2016).
30. N. Nagaosa, J. Sinova, S. Onoda, A. H. MacDonald, N. P. Ong, Anomalous Hall effect. *Rev. Mod. Phys.* **82**, 1539–1592 (2010).
31. X. Li, J. T. Mullen, Z. Jin, K. M. Borysenko, M. B. Nardelli, K. W. Kim, Intrinsic electrical transport properties of monolayer silicene and MoS_2 from first principles. *Phys. Rev. B Condens. Matter Mater. Phys.* **87**, 115418 (2013).
32. K. Kaasbjerg, J. H. J. Martiny, T. Low, A.-P. Jauho, Symmetry-forbidden intervalley scattering by atomic defects in monolayer transition-metal dichalcogenides. *Phys. Rev. B* **96**, 241411 (2017).
33. H. Liu, J. Chen, H. Yu, F. Yang, L. Jiao, G. B. Liu, W. Ho, C. Gao, J. Jia, W. Yao, M. Xie, Observation of intervalley quantum interference in epitaxial monolayer tungsten diselenide. *Nat. Commun.* **6**, 8180 (2015).
34. C. Zhang, Y. Chen, A. Johnson, M. Y. Li, L. J. Li, P. C. Mende, R. M. Feenstra, C. K. Shih, Probing critical point energies of transition metal dichalcogenides: Surprising indirect gap of single layer WSe_2. *Nano Lett.* **15**, 6494–6500 (2015).
35. G. Sallen, L. Bouet, X. Marie, G. Wang, C. R. Zhu, W. P. Han, Y. Lu, P. H. Tan, T. Amand, B. L. Liu, B. Urbaszek, Robust optical emission polarization in MoS_2 monolayers through selective valley excitation. *Phys. Rev. B Condens. Matter Mater. Phys.* **86**, 081301 (2012).
36. G. L. Frey, R. Tenne, M. J. Matthews, M. S. Dresselhaus, G. Dresselhaus, Raman and resonance Raman investigation of MoS_2 nanoparticles. *Phys. Rev. B* **60**, 2883–2892 (2000).
37. H. Li, Q. Zhang, C. C. R. Yap, B. K. Tay, T. H. T. Edwin, A. Olivier, D. Baillargeat, From bulk to monolayer MoS_2: Evolution of Raman scattering. *Adv. Funct. Mater.* **22**, 1385–1390 (2012).
38. C. Lee, H. Yan, L. E. Brus, T. F. Heinz, J. Hone, S. Ryu, Anomalous lattice vibrations of single- and few-layer MoS_2. *ACS Nano* **4**, 2695–2700 (2010).

39. B. Radisavljevic, A. Radenovic, J. Brivio, V. Giacometti, A. Kis, Single-layer MoS_2 transistors. *Nat. Nanotechnol.* **6**, 147–150 (2011).
40. Y.-T. Chen, S. Takahashi, H. Nakayama, M. Althammer, S. T. B. Goennenwein, E. Saitoh, G. E. W. Bauer, Theory of spin Hall magnetoresistance. *Phys. Rev. B* **87**, 144411 (2013).
41. T. Olsen, I. Souza, Valley Hall effect in disordered monolayer MoS_2 from first principles. *Phys. Rev. B Condens. Matter Mater. Phys.* **92**, 125146 (2015).

Acknowledgments: We would like to acknowledge fruitful discussions with J. Appenzeller and S. Datta. P.U. would like to thank H. Ochoa for useful discussions on intervalley scattering in TMDs. **Funding:** T.Y.T.H., S.Z., and Z.C. gratefully acknowledge the support of this work by NEW LIMITS, a center in nCORE, a Semiconductor Research Corporation (SRC) program sponsored by NIST through award number 70NANB17H041. P.U. would like to acknowledge the support from the Purdue University Startup Funds. **Author contributions:** Z.C. conceived and managed the research project. T.Y.T.H. designed and fabricated samples and carried out electrical measurements. T.Y.T.H., K.Y.C., P.U., and Z.C. performed theoretical analysis. S.Z. carried out material preparation and optical characterizations. All authors discussed the results and wrote the manuscript. **Competing interests:** The authors declare that they have no competing interests. **Data and materials availability:** All data needed to evaluate the conclusions in the paper are present in the paper and/or the Supplementary Materials. Additional data related to this paper may be requested from the authors.

Submitted 2 July 2018
Accepted 5 March 2019
Published 19 April 2019
10.1126/sciadv.aau6478

Citation: T. Y. T. Hung, K. Y. Camsari, S. Zhang, P. Upadhyaya, Z. Chen, Direct observation of valley-coupled topological current in MoS_2. *Sci. Adv.* **5**, eaau6478 (2019).